Lamb waves in the wavenumber-time domain: Separation of established and non-established regimes

Pierric Mora

Highlights

Lamb waves in the wavenumber-time domain: separation of established and non-established regimes

Pierric Mora

- A regularizing tensor is introduced
- It enables an effective separation into near and far fields in the wavenumber-time domain
- The established regime can be sampled optimally
- The singular (near) field can by computed in a separate and small grid

Wave Motion, Vol.103, 2021
DOI: 10.1016/j.wavemoti.2021.102736

Lamb waves in the wavenumber-time domain: separation of established and non-established regimes

Pierric Mora[a,b]

[a] *Laboratoire d'Acoustique de l'Université du Mans, LAUM - UMR 6613 CNRS, Le Mans Université, Avenue Olivier Messiaen, 72085 LE MANS CEDEX 9, France*
[b] *GERS-GeoEND, Univ Gustave Eiffel, IFSTTAR, F-44344 Bouguenais, France*

Abstract

This article deals with the dynamic response of laterally unbounded, horizontally layered plates subjected to dynamic sources applied at arbitrary locations, which is ultimately a classical problem. This response is most often obtained via a modal superposition in terms of the complex Lamb modes by casting the equations in the frequency-space domain, followed by a Fourier inversion into the space-time domain. Then again, a much less often used alternative method relies on formulating the problem directly in the time domain in terms of a modal superposition in the wavenumber domain, which is followed by a Fourier inversion into the space domain, as considered in further detail herein. This alternative can offer powerful advantages in some cases, such as dealing easily with anisotropy, or with slowly propagating waves even in the absence of damping. At the same time, however, it is beset by difficulties associated with the Fourier inversion into the space domain. As a matter of fact, during forcing, the truncation of the modal series and of the numerical integrals is hindered by poorly convergent behaviors. Here we overcome both of these difficulties by considering the asymptotic, static behavior of the integrands. We find that by introducing a regularizing term, the response can be effectively separated into near and far fields, despite the fact that these frequency-domain concepts are alien to a wavenumber-time formulation. The so-defined far field is free of sharp variations and can then be computed in a numerical grid that is optimized regarding the propagating wavelengths, which only depend on the time-spectral content of the excitation and not on its space-spectrum. Finally, we also propose a hybrid way to compute the remaining near field by combining with a non-modal formulation, expressed in the wavenumber-Laplace domain.

Keywords: Green's tensor, modal expansion, wavenumber domain, numerical Laplace transform, static asymptotics, hybrid method

1. Introduction

Modal theory provides an efficient way to express the free propagation regime of the Green's tensor of an elastic plate [1]. Although it is of common knowledge that the formalism may be stated in the space-frequency or wavenumber-time domains, in which the wavenumber and angular frequency play reversed roles of eigenvalue and parameter, the former implementation is widely used while the latter is not. The predominance of the space-frequency domain strategy can easily be understood, yet we believe that the wavenumber-time domain formulation has a potential that has been so far largely ignored and neglected. This article aims at making it more attractive by giving optimal solutions to two key issues regarding numerical costs.

Let us start with a brief overview of the pros and cons of both strategies. In the following discussion we will refer to the frequency and wavenumber domain formulations as $\mathbf{k}_n(\omega)$ and $\omega_n(\mathbf{k})$.

There are several important advantages on the side of $\mathbf{k}_n(\omega)$. First, field expressions are analytical in space, which allows for very low costs when the answer is needed at a few locations only. Second, a separation between near and far fields appears naturally through evanescent and propagating modes, which yields an expression for the free propagation whose cost does not depend on the space-spectral content of the excitation. However this $\mathbf{k}_n(\omega)$ strategy complicates significantly for 3D propagation in anisotropic materials - see [2, 3, 4] for reported implementations and [5] for a correct account of the otherwise problematic caustics. Due to the angular integral which must be evaluated numerically, it is difficult to keep costs under optimal control - a key issue for large grids. And lastly: even though it only entails rather specific applications, the frequency domain fails if very long signals are involved, such as those produced by cutoff frequencies or zero group velocity modes.

On the other hand, the $\omega_n(\mathbf{k})$ formulation is for most applications less flexible due to the numerical resolution of the wavenumber integral. As a

Email address: pierric.mora@univ-eiffel.fr (Pierric Mora)

matter of fact, when the integral is made discrete the outcome is periodic in space and thus valid only at finite times, before the fastest front reaches the borders of the spatial window, and computing the field at one point or on an entire grid has more or less the same cost. However, long time signals are not an issue, and space anisotropy is treated in a simple manner because space no longer exists in the wavenumber domain. This last strength makes $\omega_n(\mathbf{k})$ attractive when time signals of 3D anisotropic propagation are required at a large number of points, as for instance with a time reversal based signal processing for imaging purposes. The most known article about $\omega_n(\mathbf{k})$ is Ref. [6]. The reader can also find in Ref. [7] a detailed derivation, with a formalism suitable to 3D anisotropic media such as fiber reinforced composite plates. Let us cite also Ref. [8] which addresses scattering problems with a BEM/FEM coupling based on $\omega_n(\mathbf{k})$ and on the Green's tensor of a half-space in the wavenumber-time domain [9, 10, 11].

Despite these works, two key aspects for optimal control of costs remain absent in the literature. The first one is the truncation of the modal series which, unlike $\mathbf{k}_n(\omega)$, does not split into propagating and evanescent modes, but does entail an infinite number of contributions and whose convergence depends on time. The second - related - aspect is the tail-end truncation of the wavenumber integral. In essence, the problems stem from expanding the sharp behavior of the field near the source on the Fourier basis for the in-plane variables and on the modeshapes for the depth variable, which are both families of smooth functions. In the past, these issues have been bypassed by taking a big enough number of modes and by considering only bell-shaped distributions of sources with limited spectral extent. One might be frustrated that a single point should penalize the whole domain of computation, and then be tempted to believe that there should be a way to separate the field between a smooth and a sharp parts without having to rely on the concepts of propagating and evanescent modes, which are out of reach in the wavenumber-time domain. The sharp part should be non-zero only near the source for the smooth one to coincide with the exact field except in that small region of space and time. These smooth and sharp parts are what we refer to as "established" and "non-established" regimes. We prefer this terminology over the more usual adjectives "near" and "far" which refer to space-frequency-domain concepts, with a well-defined quantitative meaning attached to the evanescent modes. This work proposes a constructive way to perform such a separation and gives a quantitative definition of "established" and "non-established" in terms of the space sampling one is ready

to pay to properly compute the free regime, but which unlike for "near" and "far" does not rely on physically meaningful quantities. By free regime, or free vibrations, we refer in this work to the phase where the source has ceased acting and the wave equation has become homogeneous, whereas we call forced regime, or forced vibrations, the first phase with a non-zero source term.

We shall start by showing how to compute the field away from the vicinity of the source, whatever its space-spectral content, by relying only on the modes which are significant in the free regime. The solution developed here is inspired by a strategy described by Kausel [12, 13] to truncate the wavenumber integral of a non-modal wavenumber-frequency based formulation, which relies on subtracting a static term that captures the singular behavior.

Thereafter, we continue by applying this result to subtract the propagating field to a non-modal method to obtain the remaining non-established regime in a spatial grid limited to the vicinity of the source. For this reason we assume that the reader is familiar with non-modal methods formulated in the wavenumber-frequency domain (see Refs. [12, 13, 14, 15, 16, 17] for instance), *i.e.* methods that directly derive from Thomson's [18] and Haskell's [19] milestones. We also assume that the reader is familiar with the numerical transform method sometimes called the "exponential window method" [20], but which is actually better referred to as a numerical implementation of the Laplace transform [17].

2. Modal field in the $\mathbf{k}-t$ domain: convergence of the summation in the free and forced regimes

We briefly recall in this section the expression of the Green's tensor in terms of the Lamb modes obtained in the wavenumber domain. Thorough derivations can be found in [6, 7].

2.1. Wave equation in the space-time domain

Let us consider an elastic plate with stress-free upper and lower boundaries. The plate is invariant in the $\mathbf{x} = (x, y)$ plane that contains its interfaces, but may be arbitrarily layered between $z = 0$ and $z = H$. At time $t = 0$ a dynamic load $\mathbf{b} = (b_x, b_y, b_z)^T$ appears and gives rise to wave propagation

phenomena that can be described by:

$$\begin{aligned} \rho\partial_t^2\mathbf{u} - \mathbf{L}^T\boldsymbol{\sigma} &= \mathbf{b}, && \text{(1a)} \\ \boldsymbol{\sigma} &= \mathbf{C}\boldsymbol{\varepsilon}, && \text{(1b)} \\ \boldsymbol{\varepsilon} &= \mathbf{L}\mathbf{u}, && \text{(1c)} \\ \boldsymbol{\sigma}_z &= \mathbf{0} \quad \text{at } z = 0 \text{ and } z = H, && \text{(1d)} \end{aligned}$$

where ρ is the density, $\mathbf{C} = \{C_{ij}\}_{i,j=1..6}$ the stiffness tensor, $\mathbf{u} = (u_x, u_y, u_z)^T$ the displacement, $\boldsymbol{\varepsilon} = (\varepsilon_x, \varepsilon_y, \varepsilon_z, \gamma_{yz}, \gamma_{xz}, \gamma_{xy})^T$ the strain, $\boldsymbol{\sigma} = (\sigma_x, \sigma_y, \sigma_z, \sigma_{yz}, \sigma_{xz}, \sigma_{xy})^T$ the stress, $\boldsymbol{\sigma}_z = (\sigma_{xz}, \sigma_{yz}, \sigma_z)^T$ the normal stress and

$$\mathbf{L}^T = \begin{bmatrix} \partial_x & 0 & 0 & 0 & \partial_z & \partial_y \\ 0 & \partial_y & 0 & \partial_z & 0 & \partial_x \\ 0 & 0 & \partial_z & \partial_y & \partial_x & 0 \end{bmatrix} \tag{2}$$

a differential operator. Equations (1) must also be complemented with a set of continuity conditions on $\mathbf{u}$ and $\boldsymbol{\sigma}_z$ at the interfaces where the mechanical properties ρ and $\mathbf{C}$ are discontinuous. For the sake of clarity we assume that space and time dependence of the source can be separated: $\mathbf{b} = f(t)\,\boldsymbol{\psi}(\mathbf{x}, z)$, although the further developments can be equally applied to moving sources. The excitation signal $f(t)$ will be the driving quantity in the following, whereas $\boldsymbol{\psi}$ hardly plays a role.

If in Eq. (1a) the load is replaced by a set of impulsive loads $\mathbf{b} \to \delta(\mathbf{x})\delta(z - z')\delta(t)\ \mathbf{I}_3$, with $\mathbf{I}_3$ the 3×3 identity matrix, then the displacement response at point $(\mathbf{x}, z, t)$ is the Green's tensor $\mathbf{g}(\mathbf{x}, z, z', t) = \{g_{ij}\}_{i,j=x,y,z}$ of the problem and may be post-treated to obtain the solution to the original problem with load $\mathbf{b}$:

$$\mathbf{u} = \mathbf{g} * \mathbf{b}. \tag{3}$$

The strategy which is adopted in this work to obtain $\mathbf{g}$ is to Fourier-transform the plane variable $\mathbf{x} \to \mathbf{k}$, to solve the resulting PDE on t and z to obtain the Green's tensor $\mathbf{G}(\mathbf{k}, z, z', t)$ at each point $\mathbf{k} = (k_x, k_y)^T$ of a grid that remains to be specified, and to finally back-transform by numerical Fourier synthesis:

$$\mathbf{g}(\mathbf{x}, z, z', t) = \mathcal{F}^{-1}\{\mathbf{G}(\mathbf{k}, z, z', t)\}. \tag{4}$$

Proper truncation of the wavenumber integral (4) is the ultimate goal of this article. Inversion (4) is a 2D integral if the response to a point load is required, but can be simplified to a 1D integral using cylindrical coordinates

if the plate is planar-isotropic. Naturally, if the required outcome is the response to a line load - as will be the case in the examples, $\mathbf{k}$ must be read as a scalar and inversion (4) is a 1D integral.

2.2. Green's tensor of an elastic plate in the $\mathbf{k}-t$ domain

In the $\mathbf{k}$ domain, the differential operator $-\mathbf{L}^T\mathbf{C}\mathbf{L}/\rho$ that appears after inserting Eqs. (1b) and (1c) into Eq. (1a) and dividing each side by ρ is self-adjoint when acting on functions satisfying Eq. (1d). It may be expanded over its eigenbasis, which are the Lamb modes of the plate. Several techniques exist to calculate the modes for an arbitrary layering. Those which rely on an analytical account of the z dimension through the use of the basis of bulk waves in each layer must face the difficult task of solving a transcendental equation $\det\{\text{System}\}(\omega_n) = 0$. On the other hand, those which rely on discretizing z only need to call a solver to find the eigenvalues and eigenvectors of finite difference or finite element matrices. These last techniques are extensively described in the references mentioned above.

Assuming that at a given $\mathbf{k}$ the angular eigenfrequencies ω_n and mode-shapes $\mathbf{U}_n(z)$ are known[1], $\mathbf{G}$ can be expressed as a modal summation:

$$\mathbf{G} = \sum_{n=0}^{+\infty} g_n(t)\ \mathbf{U}_n(z)\ \mathbf{U}_n^\dagger(z'). \tag{5}$$

In Eq. (5) $\dagger$ refers to the conjugate transpose and g_n is the modal propagator:

$$g_n(t) = \mathcal{H}(t)\ \frac{\sin\ \omega_n\, t}{\omega_n}, \tag{6}$$

$\mathcal{H}$ being the Heaviside unit step function. Equation (6) changes to $g_n = \mathcal{H}(t)\, t$ for rigid body motions $\omega_n = 0$. Notice that because of the causal door $\mathcal{H}(t)$, g_n is not monochromatic, but broad band. This is an essential feature to understand the good or poor convergence on n of summation (5).

Equation (5) is evaluated on a grid in $\mathbf{k}$ whose steps relate to the dimensions of the spatial domain of interest, and whose upper limits will be specified further. Finally, inversion (4) and convolution (3) can be applied. Notice that the spatial part of convolution (3) is usually performed directly in the wavenumber domain.

[1] $\mathbf{U}_n$ must be normalized: $\int_0^H \rho\, ||\mathbf{U}_n||^2\, \mathrm{d}z = 1$

The important question that remains regarding Eq. (5) is: Given a source term, how many modes are needed in the summation? Compared to a formulation in the frequency domain the answer is not as straightforward: evanescent modes do not exist and the modal expansion only involves real wavenumbers - by construction - and real frequencies - as a result of the self-adjoint nature of the differential operator in the $\mathbf{k}$ domain (see Ref. [7] for a proof). The series does not admit a separation between propagative modes in finite number and non-propagative terms in infinite number. This makes the convergence of summation (5) time-dependent, as will be emphasized in the next two paragraphs.

2.3. Optimal sampling in the free regime

In this section we first assume for simplicity that the space distribution of the load is point-wise: $\mathbf{b} = \delta(\mathbf{x})\,\delta(z-z_0)\,f(t)\,\boldsymbol{\psi}$, with $\boldsymbol{\psi}$ a constant vector. This consideration will lead us to obtain a criterion to truncate the wavenumber integral (4) and modal summation (5) which is valid for the free regime and is optimal in this adverse case where the sharpness of the source does not help the integrand to decrease at high wavenumbers or high modal order. This criterion will then be used as a safe upper bound for the general case of smoother, distributed loads, and will serve as an objective to reach for the developments presented in the following sections.

In the $\mathbf{k}-t$ domain the spatial part of convolution (3) expresses as $\mathbf{b}_n(z) = \mathbf{U}_n(z)\,\mathbf{U}_n^\dagger(z_0)\,\boldsymbol{\psi}$. While its exact magnitude depends on the source and receiver locations z and z_0, it can be shown in a number of special cases (e.g. a shear-horizontal motion with $z = z_0 = 0$) that $||\mathbf{b}_n(z)||$ may be constant with $\mathbf{k}$ and n. In any case, one cannot rely on the asymptotic behavior of $||\mathbf{b}_n(z)||$ to ensure the convergence of integral (4) and summation (5). As will be emphasized now, a key aspect in this regard is the temporal part of the convolution.

If the source vanishes after some time t_{end}, *i.e.* if $f(t > t_{end}) = 0$, then the convolution with the modal propagator reaches a stationary, harmonic form. Indeed,

$$\{g_n * f\}(t) = \mathrm{Im}\left\{\int_{-\infty}^{t} f(\tau)\,\frac{\mathrm{e}^{\mathrm{i}\,\omega_n(t-\tau)}}{\omega_n}\,\mathrm{d}\tau\right\}, \tag{7}$$

the upper bound of which becomes constant and can be replaced by $t \to t_{end}$ as soon as $t \geq t_{end}$. The $\mathrm{e}^{\mathrm{i}\,\omega_n t}/\omega_n$ term can be pulled out of the integral, one recognizes the definition of the Fourier transform $\mathcal{F}\{f\}(\omega_n) =$

$\int f(\tau)\,\mathrm{e}^{-\mathrm{i}\omega_n\tau}\,\mathrm{d}\tau$, and Eq. (7) finally expresses as

$$\{g_n * f\}(t) = \mathrm{Im}\left\{\frac{\mathcal{F}\{f\}(\omega_n)\,\mathrm{e}^{\mathrm{i}\,\omega_n\,t}}{\omega_n}\right\} \text{ if } t \geq t_{end}. \tag{8}$$

Equation (8) shows that the modes with eigenfrequencies lying outside the spectrum of the source term do not contribute to the free regime. Let us give a name to this maximal angular frequency, as it will play a pivoting role throughout the remainder of this article: given a desired numerical precision regarding the free regime, ω_{max} is such that $|\mathcal{F}\{f\}(\omega > \omega_{max})|/\omega \approx 0$, and hence $\omega_n > \omega_{max}$ can be ignored in the modal summation for $t \geq t_{end}$[2]. As a consequence, the Fourier integral on $\mathbf{k}$ can be optimally truncated to the region where the lowest mode is such that $\omega_0(\mathbf{k}) \leq \omega_{max}$. In isotropic homogeneous plates the high-frequency asymptotics of this optimal sampling is $||\mathbf{k}|| \leq k_{max}$ with the Nyquist wavenumber $k_{max} = \omega_{max}/c_R$, c_R being the Rayleigh wave velocity. More generally, let us call $||\mathbf{k}|| \leq k_{max}(\omega_{max}, \theta)$ the optimal Nyquist wavenumber for the free regime, θ being the direction of the wavevector.

Of course, if the source is smoothly distributed in $\mathbf{x}$ or z, then the "optimal" Nyquist wavenumber k_{max} defined here is an over-estimation of the truly optimal sampling. In the case where the load is smooth along $\mathbf{x}$, k_{max} can be easily refined by accounting for the given space-spectrum. If the load is smooth along z, then the proper way to refine k_{max} is to define it as explained upper after having excluded the modes that are not excited. These refinements are left to the reader - in this work k_{max} will be constructed based on the mode having slowest phase velocity at ω_{max}.

We highlight that the level at which $|\mathcal{F}\{f\}(\omega > \omega_{max})|/\omega \approx 0$ is neglected is the guideline for making a truncation that only results in an approximation in space, in the sense that it leads to spatial sub-sampling, but not in time. Indeed, the time-convolution can still independently be evaluated with an arbitrary precision, or even analytically for canonical input signals. The purpose of this comment is to make clear that anti-causal artifacts - such as those resulting from a coarse time sampling - are not generated with a low threshold of $\omega_n < \omega_{max}$, so that one can still rely on a numerical Laplace transform to evaluate the time convolution, which is more demanding in

[2] t_{end} and ω_{max} are not related: although it is clear that ω_{max} cannot be much smaller than $2\,\pi/t_{end}$, it can in principle be arbitrarily larger.

spectral accuracy than a mere Fourier transform. This comment will be illustrated with an example below.

2.4. Static singularity in the forced regime

However, things are different during the forced regime, when the source is not zero. Indeed, the condition imposed by the heterogeneous member in Eq. (1a) is a jump of the stress across the origin in the direction of the load. The field is then sharp, its space derivative is discontinuous and the space derivative of the stress is singular. This behavior is bound to the presence of the load and disappears as soon as the excitation has disappeared. In this sense it is a static singularity. To see it in the formalism of normal modes let us transform the time domain into the Laplace domain:

$$\mathcal{L}\{g_n * f\}(s) = \frac{\mathcal{L}\{f\}(s)}{\omega_n^2 + s^2}. \tag{9}$$

In the limit $\omega_n \gg |\mathrm{Im}(s)|$, Eq. (9) leads to $\mathcal{L}\{g_n * f\}(s) \approx \mathcal{L}\{f\}(s)/\omega_n^2 + \mathcal{O}(s^2/\omega_n^2)$ and therefore to $(g_n * f)(t) \approx f(t)/\omega_n^2$. The response is then in this limit directly proportional to the excitation, which is indeed a static behavior. This means that whatever the time-spectrum of the source, the contribution of high modal frequencies decreases slowly while $f(t)$ is not zero. To be more accurate, let us perform a series expansion of Eq. (9):

$$\mathcal{L}\{g_n * f\}(s) \approx \sum_{m\geq 0} (-1)^m \frac{s^{2\,m}\mathcal{L}\{f\}(s)}{\omega_n^{2\,m+2}}. \tag{10}$$

Equation (10) can be back-transformed to the time domain as:

$$(g_n * f)(t) \approx \sum_{m\geq 0} (-1)^m \frac{\partial_t^{2\,m} f(t)}{\omega_n^{2\,m+2}}. \tag{11}$$

We can then see from Eq. (11) that memoryless terms - proportional to time-derivatives - contribute as increasing powers of $1/\omega_n$. By "memoryless" we mean a response that is not directly proportional to the excitation, but disappears as soon as the excitation disappears as for a static behavior. As long as $\omega_n = \omega_n(\mathbf{k})$ depends on the wavenumber, this slow convergence also has a consequence on the truncation of the Fourier integral on $\mathbf{k}$. In other words, if one keeps the sampling $||\mathbf{k}|| \leq k_{max}$ which is optimal for the free field to synthetise the forced regime, then the neglected part will be significant

and the outcome will suffer a severe spatial aliasing. The artifact will not be contained in the neighborhood of the source but rather slowly decreases with space.

Let us close this section with the following comment on Eq. (11): if one assumes a non-dispersive relation $\omega_n \propto k$ - which is anyway the asymptotics of every modal branch - then one sees that a time derivative ∂_t^{2m} is associated with a $1/k^{2m+2}$ decrease. After an inverse Fourier transform on k, this power-law decrease is in turn characteristic of a discontinuity at $x = 0$ of the $(2m+1)^{th}$ space-derivative. Equation (11) may therefore be interpreted as a sum of terms of increasing regularity in space, the lowest order ones of which being are the most problematic.

2.5. An illustrating case: transient motion of Shear-Horizontal modes

Before going further let us illustrate the former paragraphs with a case which can be carried out analytically (see Ref. [21] for instance). Consider a homogeneous and isotropic plate of thickness H, shear wave velocity c_S and mass density ρ, which is subjected to a brief anti-plane line load in the y direction, $b_y = f(t)\,\delta(x)\,\delta(z)$, acting on the upper surface that contains the origin of coordinates (see Fig.1-(a)). Other than the applied load, both the upper and lower surfaces are stress free. The resulting motion $\mathbf{u}(x,z,t) = (0,u_y,0)^T$ is then purely shear and Eqs. (1) take the simpler form:

$$\begin{aligned} \partial_t^2 u_y - c_S^2(\partial_x^2+\partial_z^2)u_y &= \rho^{-1} b_y, && \text{(12a)} \\ \mu\partial_z u_y &= 0 \quad \text{at } z=0 \text{ and } z=H. && \text{(12b)} \end{aligned}$$

In the wavenumber domain, the differential operator $-c_S^2(\partial_z^2 - k^2)$ acting on functions satisfying boundary conditions (12b) has the following eigenmodes:

$$\begin{aligned} \omega_n &= c_S\sqrt{k^2+(n\pi/H)^2}, && \text{(13a)} \\ U_n &= \frac{1}{\sqrt{\rho H}}\cos\left(\frac{zn\pi}{H}\right)\times\begin{cases}1, & \text{if } n=0,\\ \sqrt{2}, & \text{if } n\geq 1.\end{cases} && \text{(13b)} \end{aligned}$$

These eigenfunctions can be analytically back-transformed to the space domain, yielding the following normal-mode expansion for the Green's function of Eqs (12):

$$\begin{aligned} u_y(x,z,t) &= g * b_y, && \text{(14a)} \\ g(x,z,z',t) &= \sum_{n\geq 0} g_n, && \text{(14b)} \end{aligned}$$

thickness	density	Lamé's constants	bulk velocities
$H = 1$ mm	$\rho = 2.7$ g/cm^3	$\lambda = 58$	$c_P \approx 6.27$
		$\mu = 24$ GPa	$c_S \approx 2.98$ mm/μs

Table 1: Parameters of the aluminum plate considered in the examples

with

$$g_n(x, z, z', t) = \frac{U_n(z)U_n(z')}{2c_S}\ \mathcal{H}(t - |x|/c_S)\ \mathrm{J}_0\left(\frac{n\pi c_S}{H}\sqrt{t^2 - x^2/c_S^2}\right), \quad (15)$$

where J_0 is the Bessel function of first kind and order 0. The solution (15) is particularly simple for the fundamental mode $n = 0$. In this case the convolution with the excitation also has a closed form expression:

$$\{g_0 * f\}(x, z, z', t) = \frac{c_S}{2\mu H}\int_0^{t-|x|/c_S} f(\tau)\ \mathrm{d}\tau. \quad (16)$$

Let us now go to an example. The plate under consideration in this section and for the remainder of this article will be a single layer of (poly-cristaline) aluminum (see Tab. 1). As for a source term we take a 2D-point-wise Ricker impulse:

$$b_y = f(t)\ \delta(x)\ \delta(z'), \quad (17a)$$

$$f(t) = \left(1 - \frac{(t - t_0)^2}{\tau_e^2}\right)\exp\left(-\frac{(t - t_0)^2}{2\tau_e^2}\right), \quad (17b)$$

where τ_e defines the duration of the excitation - it is roughly one quarter of the dominant period - and t_0 stands for the time at which the impulse is applied - taken positive to ensure causality for numerical evaluation of convolutions.

The spectral extent of this source is white in space $\mathcal{F}\{\delta(x)\}(k) = 1$. The modal participation factors $b_n = \int_0^H b_y(z)\ U_n(z)\ \mathrm{d}z$, which from Eq. (13b) are the cosine transform of the depth-extent of the source at wavenumbers $k_{z,n} = n\pi/H$, are all equal to unity (times the normalization factor which is constant for $n \geq 1$). The time-spectrum of b_y is of the form $|\mathcal{F}\{f\}(\omega)| = \omega^2\tau_e\sqrt{2\pi}\exp(-\omega^2\tau_e^2/2)$. A preliminary evaluation of $|\mathcal{F}\{f\}(\omega)/\omega|$ is summarized in Tab. 2 as a guideline to define the thresholds ω_{max} and Nyquist wavenumbers $k_{max}(\omega_{max})$ later on according to a desired numerical precision.

magnitude	1	10^{-1}	10^{-2}	10^{-3}	10^{-4}	10^{-5}	10^{-6}	10^{-7}
$\omega \times \tau_e/2\pi$	0.16	0.44	0.57	0.67	0.76	0.83	0.90	0.97

Table 2: Numerical study of the spectrum of the primitive of the excitation $|\mathcal{F}\{f\}(\omega)|/\omega$: values of ω reaching different magnitudes as possible definitions for ω_{max}.

The duration τ_e is chosen such that the free regime is dominated by the first two modes SH_0 and SH_1. We take $\tau_e = 0.25$ μs. The time-offset t_0 is chosen such that the excitation is negligible at $t = 0$, because time-convolutions in the space domain with modes $n \geq 1$ are to be evaluated numerically from Eq. (15). We take $t_0 = 6\,\tau_e = 1.5$ μs. Concerning time-convolutions in the wavenumber domain, the following formula can be established:

$$\left\{\mathcal{H}(t)\,\frac{\sin\omega_n t}{\omega_n} * f\right\}(t+t_0) = -\tau_e^2 \mathrm{e}^{-t^2/2\tau_e^2} + \omega_n \tau_e^3 \sqrt{\frac{\pi}{2}}\,\mathrm{Im}\left\{\mathrm{e}^{\mathrm{i}\omega_n t - \omega_n^2\tau_e^2/2} \times \left[1 + \mathrm{erf}\left(\frac{t}{\tau_e\sqrt{2}} + \mathrm{i}\,\frac{\omega_n\tau_e}{\sqrt{2}}\right)\right]\right\}. \quad (18)$$

The relevant dispersion curves are represented in Fig. 1 together with the spectra of the source term. The field is represented in Fig. 2 at depth $z = 0$ at two instants, during the forced regime at t_0 when the excitation is maximal, and then at $t_1 = t_0 + 6\,\tau_e = 3$ μs when the excitation can be reasonably considered to be finished and the regime to be free. The curves are normalized by the amplitude of the fundamental mode in the free regime. As can be seen, the free regime can be described with only the first two modes if relative contributions lower than 10^{-4} are neglected. According to Tab. 2, this would be consistent with a threshold $\omega_{max}^{(1e-4)} = 0.76 \times 2\pi/\tau_e = 19.1$ rad MHz and results of the same quality could be obtained by a numerical resolution of the wavenumber integral sampled with a Nyquist wavenumber $k_{max}^{(1e-4)} = \omega_{max}^{(1e-4)}/c_S = 6.4$ rad/mm. On the other hand, the forced regime would clearly be problematic for such a resolution if nothing were done. Indeed, a very high number of modes contribute due to the z-sharp source, and each branch requires in turn a very high Nyquist wavenumber due to the x-sharp source. How then to decide on proper criteria for the truncations?

3. Removing the singular part of the Green's tensor

The goal of this section is to construct a regularizing tensor - let us call it $\tilde{\mathbf{g}}^{(S)}$ - with the same singular behavior as $\mathbf{g}$. The desired form of $\tilde{\mathbf{g}}^{(S)}$ must

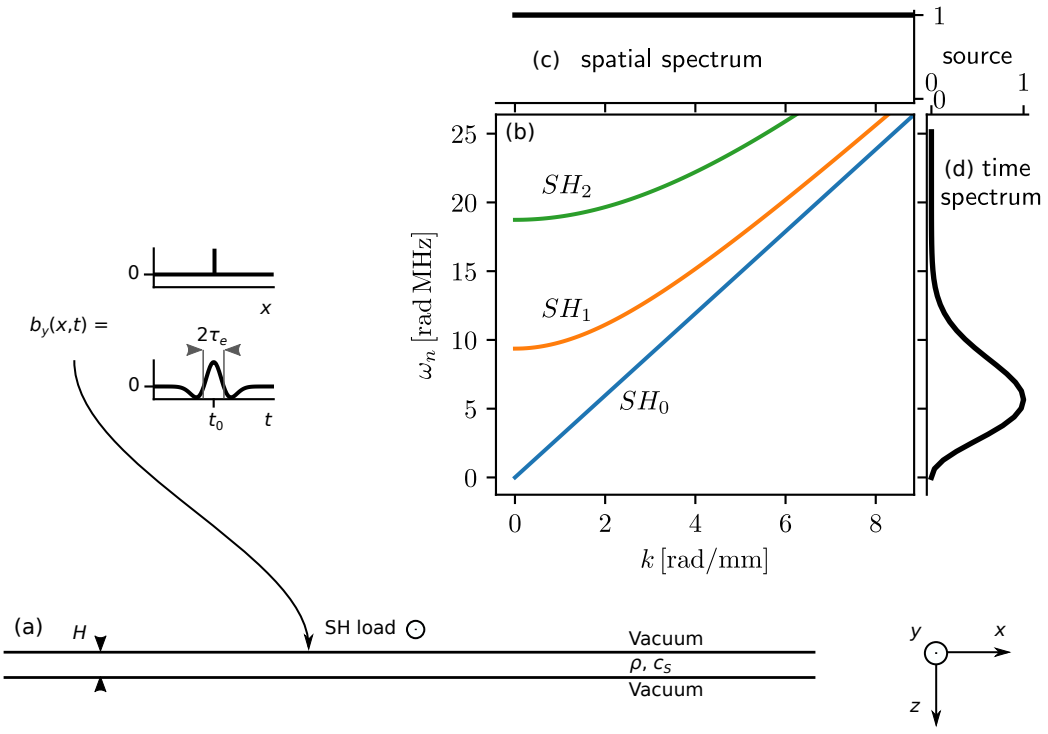

Figure 1: (a) Scheme of the configuration for SH examples. (b) Dispersion curves of the first SH modes of a 1 mm-thick aluminum plate. (c) Spatial- and (d) time-spectra of a 2D point-wise Ricker impulse.

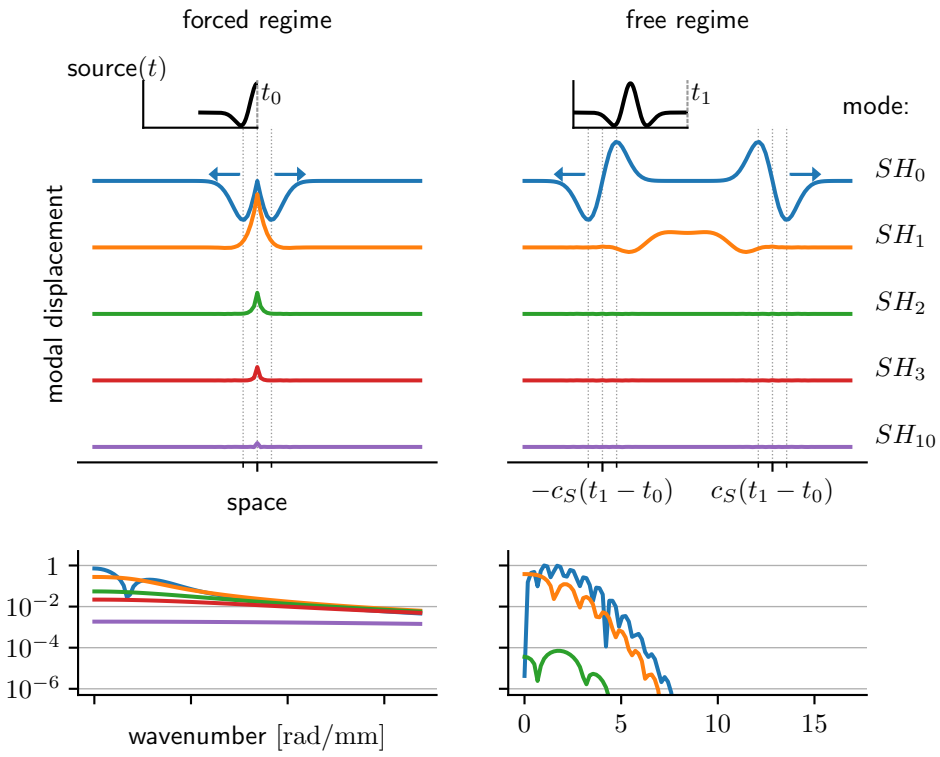

Figure 2: Space and wavenumber snapshots of a shear motion during the forced and free regimes, showing the poor convergence of the modal series and the slow decrease of wavenumber integrands during excitation due to the sharp behavior at the origin. The space-fields are computed from space-domain Green's functions.

be such that the regularized (or established) field $\tilde{\mathbf{u}} \equiv (\mathbf{g} - \tilde{\mathbf{g}}^{(S)}) * \mathbf{b}$ can be expanded in the $\mathbf{k}$-domain over a modal series truncated at $\omega_n < \omega_{max}$ and sampled with $||\mathbf{k}|| \leq k_{max}$ even during the forced regime, while the residual (or non-established) field $\mathbf{u} - \tilde{\mathbf{u}}$ is contained in the vicinity of the source. $\tilde{\mathbf{g}}^{(S)}$ will be constructed as a sum of memoryless terms: a static part plus terms proportional to time derivatives. This way, the residual field $\mathbf{u} - \tilde{\mathbf{u}}$ will be non-zero only when the source is non-zero.

3.1. Definition of $\tilde{\mathbf{g}}^{(S)}$ in the wavenumber-time and wavenumber-Laplace domains

A natural idea is to keep the same spatial part as $\mathbf{g}$, that is, the projection of a point source over the normal modes. Concerning the time behavior however, one cannot simply take a static version of Eq. (9), *i.e.* with $s = 0$, because of the singularities that would appear at $\omega_n = 0$.

Let us express $\tilde{\mathbf{G}}^{(S)}(\mathbf{k}) = \mathcal{F}\{\tilde{\mathbf{g}}^{(S)}(\mathbf{x})\}$ through Eq. (5) by formally replacing $g_n \to \tilde{g}_n^{(S)}$:

$$\tilde{\mathbf{G}}^{(S)} \equiv \sum_{n=0}^{+\infty} \tilde{g}_n^{(S)}(t)\ \mathbf{U}_n(z)\ \mathbf{U}_n^{\dagger}(z'). \tag{19}$$

Let us then define $\tilde{g}_n^{(S)}$ in a way inspired by Eq. (11). In the Laplace domain, we write:

$$\mathcal{L}\{\tilde{g}_n^{(S)}\}(s) \equiv \sum_{m\geq 0} (-1)^m \frac{s^{2\,m}}{\tilde{\omega}_{mn}^{2\,m+2}}, \tag{20}$$

or equivalently in the time domain:

$$\tilde{g}_n^{(S)}(t) \equiv \sum_{m\geq 0} (-1)^m \frac{\partial_t^{2\,m}}{\tilde{\omega}_{mn}^{2\,m+2}}, \tag{21}$$

in which the function $\tilde{\omega}_{mn} = \tilde{\omega}_{mn}(m, \omega_n, \omega_{max})$ and the number of terms must still be specified.

The problem is now to find a suitable definition for $\tilde{\omega}_{mn}$. Two features are essential:

- $\tilde{\omega}_{mn} - \omega_n \to 0$ smoothly enough in the limit $\omega_n \to \omega_{max}$ to regularize the truncation of the space Fourier integral,
- $\tilde{\omega}_{mn}|_{\omega_n=0} \neq 0$ to avoid a singular behavior.

Furthermore, two other features are desirable:

- The spectrum of $\tilde{\omega}_{mn}^{2\,m+2} - \omega_n^{2\,m+2}$ viewed as a function of ω_n should be confined to frequencies as low as possible, for $\mathbf{u} - \tilde{\mathbf{u}}$ to be confined to a region of space as small as possible. Indeed, if we write the following approximation for the difference of propagators considering both $\omega_n \gg |\mathrm{Im}(s)|$ and $\omega_n, \omega_{mn} \approx \omega_{max}$:

$$\begin{aligned} \mathcal{L}\{g_n - \tilde{g}_n^{(S)}\}(s) &\approx \sum_{m\geq 0} s^{2\,m}(-1)^m \left(\frac{1}{\omega_n^{2\,m+2}} - \frac{1}{\tilde{\omega}_{mn}^{2\,m+2}}\right), \\ &\approx \sum_{m\geq 0}(-1)^m \frac{s^{2\,m}}{\omega_{max}^{2\,m+2}} \; \frac{\tilde{\omega}_{mn}^{2\,m+2} - \omega_n^{2\,m+2}}{\omega_{max}^{2\,m+2}}, \end{aligned} \tag{22}$$

  we can see that the behavior of the wavenumber integral may be controlled by controlling the spectrum of $\tilde{\omega}_{mn}^{2\,m+2}(\mathbf{k}) - \omega_n^{2\,m+2}(\mathbf{k})$. A simple way to establish a guideline is then to assume a non-dispersive relation $\omega_n \propto ||\mathbf{k}||$ in the former equation.

- The ratio $(\omega_{max}/\tilde{\omega}_{mn})^{2\,m+2}$ should decrease with m, with a particular care for $\omega_n \ll \omega_{max}$ where Eq. (11) does not hold and subtracting $\tilde{g}_n^{(S)}$ to g_n mainly introduces spurious contributions. Indeed, ω_{max} represents the level at which the time-spectrum of the excitation may be neglected and defines this way the overall numerical approximation. Increasing m means performing time-derivatives which push the energy content of the spectrum towards higher frequencies. Neglecting these spectra at the same frequency threshold will eventually conflict with the original approximation. On the one hand, such a problematic time-derivation may be measured by $\times\omega_{max}$, while on the other hand the magnitude of spurious $\partial_t^{2\,m}$ introduced by $\tilde{g}_n^{(S)}$ is at most $1/\tilde{\omega}_{mn}^{2\,m+2}$, so in order to avoid causality to be degraded and keep numerical errors under control, a safe requirement is that this ratio should decrease with m.

Following these guidelines, we define $\tilde{\omega}_{mn}$ as:

$$\tilde{\omega}_{mn} = \omega_{max}\; \tilde{\Omega}_m(\omega_n/\omega_{max}), \tag{23a}$$

$$\tilde{\Omega}_m^{2\,m+2}(\Omega) = \Omega^{2\,m+2} + \gamma_m\, \mathrm{W}(\Omega), \tag{23b}$$

W being a normalized window function defined for $\Omega \in [0,1]$ and $\{\gamma_m\}_{m\geq 0}$ a sequence of numbers. In the examples we mostly use a Hann window. When required by an illustrating case we extend $W(\Omega > 1) = 0$. As for $\{\gamma_m\}_{m\geq 0}$,

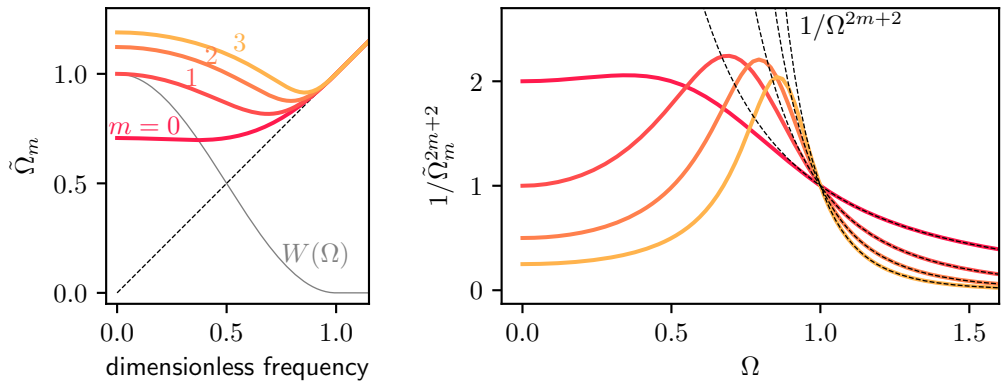

Figure 3: First orders functions $\tilde{\Omega}_m(\Omega)$ used to construct the regularizing term.

although we do not see for the moment a clear recipe to decide on its values, the following formula yielded best results out of several empirical trials:

$$\gamma_m = 2^{m-1}. \tag{24}$$

The functions $\tilde{\Omega}_m(\Omega)$ are represented in Fig. 3 for the first values of m. The spatial parts $\tilde{g}_m^{(S)}(x) \equiv \mathcal{F}^{-1}\{\tilde{\Omega}_m^{-(2m+2)}(k)\}$ of the regularizing term $\tilde{\mathbf{g}}^{(S)}$ are represented in Fig. 4 assuming a non-dispersive relation $\Omega = k/k_{max}$. They were computed by Fourier synthesis with a high enough Nyquist wavenumber ($k_N = 10\ k_{max}$, *i.e.* $\Omega \leq 10$). Notice that the purpose is purely pedagogical because the normal use should be to truncate wavenumber integrals on $\mathbf{G} - \tilde{\mathbf{G}}^{(S)}$ at $\Omega = 1$ instead of evaluating $\tilde{g}_m^{(S)}(x)$ alone. Regarding Fig. 4, let us make two comments. First, the lowest order $\tilde{g}_0^{(S)}$ clearly has the expected sharp behavior at the origin. The three others would look similar after respectively 2, 4 and 6 space-derivations. Second, even though these functions become wider as m grows due to their increased spectral localization near $\Omega = 1$ as a result of the sequence $\{\gamma_m\}$, they remain localized within what would be a few space-samples if the Nyquist wavenumber were $k_N = k_{max}$ (*i.e.* $\Omega = 1$ and $\delta x = \pi/k_{max}$). So, at first glance these functions seem to meet our requirements.

3.2. Performance of $\tilde{\mathbf{g}}^{(S)}$ as a regularizing term: numerical examples

3.2.1. Example 1: transient SH motion

Let us start with the same configuration as in Section 2.5. The fields are now evaluated in the wavenumber domain, regularized in the sense defined

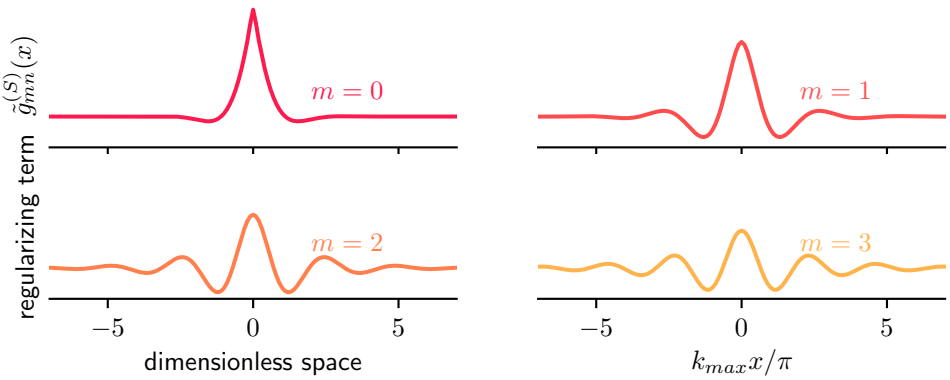

Figure 4: First orders regularizing terms back-transformed to the space domain assuming a non-dispersive relation $\omega_n = c\ k$.

in the previous section, and then back-transformed by Fourier synthesis to a space window $\{-x_{max}, x_{max} + \delta x, ..., x_{max} - \delta x\}$ of a desired length $2x_{max}$ by sampling Eq. (4) at $k = \{0, \delta k, 2\delta k, ..., k_N\}$, with $\delta k = \pi/x_{max}$ and $k_N = \pi/\delta x$ a Nyquist wavenumber chosen immediately above the threshold k_{max} (to be specified) so that the number of points in space $2x_{max}/\delta x$ is even. The fields are then zero-padded for smoother rendering. The outcome of this procedure is superscripted $^{<\text{opt}>}$, for "optimally sampled" (in the sense defined in Section 2.3), and is hence named $\tilde{\mathbf{u}}^{<\text{opt}>}$. It is compared to the exact field $\mathbf{u}$ computed as in Section 2.5, so that the residual field $\mathbf{u} - \tilde{\mathbf{u}}^{<\text{opt}>}$ can also be studied. The fields are to be computed at the same instants $t_0 = 1.5$ μs and $t_1 = 3$ μs as before, so the halved size of the space window is set at $x_{max} = c_S(t_1 - t_0 + 5.5\,\tau_e) \approx 8.6$ mm to avoid contamination from periodized sources.

The "true" field $\mathbf{U}(k, z, t)$ is evaluated with Eqs. (5), (6), (13) over the SH modes having angular frequencies lower than ω_{max} (to be specified), and the time-convolution is performed analytically with Eq. (18). The regularizing field $\tilde{\mathbf{U}}^{(S)}(k, z, t)$ is defined according to Eqs. (23) and (24) with parameters that will be specified further and evaluated directly in the time domain using Eq. (21) and:

$$\partial_t^{2m} f(t) = -\tau_e^{-2m} \mathsf{He}_{2m+2}\left(\frac{t - t_0}{\tau_e}\right) \exp\left(-\frac{(t - t_0)^2}{2\tau_e^2}\right), \tag{25}$$

in which He_m is the "probabilists'" Hermite polynomial of degree m.

We first focus on the simplest, lowest order SH_0 mode to perform several

parametric studies. For this mode neither the depth of excitation z' nor that of reception z play a role. The exact solution is given by Eq. (16).

We start with a study on ω_{max} which defines the truncation threshold for the modal basis, the Nyquist wavenumber $k_{max} = \omega_{max}/c_S$, and is a parameter of the regularizing frequency $\tilde{\omega}_{mn}$. ω_{max} is varied in $\{0.4, 0.7, 1, 2\} \times 2\pi/\tau_e \approx \{10.1, 17.6, 25.1, 50.3\}$ rad MHz, which according to Tab. 2 means neglecting relative contributions below $\{0.17, 5 \times 10^{-4}, 3 \times 10^{-8}, 10^{-33}\}$ in the free regime. The first and last thresholds stand for exaggerated values while the second and third ones are representative values of, say, moderate and high accuracy requirements. The corresponding values for k_{max} are $\{3.4, 5.9, 8.4, 16.9\}$ rad/mm. The other parameters are kept constant: W is a Hann window and summation (21) is cut at $m \leq 3$. The results are represented in Fig. 5 in solid lines. The exact solution is displayed in dotted line. One can clearly see that subtracting $\tilde{\mathbf{U}}^{(S)}$ indeed results in smoothing the sharp behavior around the origin during the forced regime without affecting the solution away from a contained region where the residual field decreases exponentially. The size of this region can be controlled at will with ω_{max}. One also sees that $\tilde{\mathbf{U}}^{(S)}$ is zero in the free regime so that the field is exact up to the numerical precision defined by ω_{max}. This example hence demonstrates the leading role of ω_{max} in the quantitative definition of what "established" and "non-established" regimes mean in a similar way with which evanescent modes give a quantitative meaning to "far" and "near" fields.

We now investigate the influence of two other parameters, namely the number of terms included in summation (21) that defines $\tilde{g}_n^{(S)}$ - varied between none and 5, and the window function W introduced in Eq. (23b) to define $\tilde{\omega}_{mn}$ - chosen of increasing smoothness as triangular[3], Hann[4] and Nuttall[5] windows. The other parameters are kept constant: $\omega_{max} = 1 \times 2\pi/\tau_e \approx 25.1$ rad MHz and $k_{max}(\omega_{max}) \approx 8.4$ rad/mm. The results are represented in Fig. 6. It clearly appears that a triangular window is too sharp to give satisfactory results, even if many terms are included in summation. The Hann window performs better because it achieves a good compromise in the spectral domain between a thin primary lobe and a low plateau of secondary

[3] $\mathrm{W}(\Omega) = 1 - |\Omega|$

[4] $\mathrm{W}(\Omega) = \cos^2(\pi\,\Omega/2)$

[5] $\mathrm{W}(\Omega) = \sum_{q=0}^{3} a_q \cos(q\,\pi\,\Omega)$, with $a_0 \approx 0.355768$, $a_1 \approx 0.487396$, $a_2 \approx 0.144232$, $a_3 \approx 0.012604$

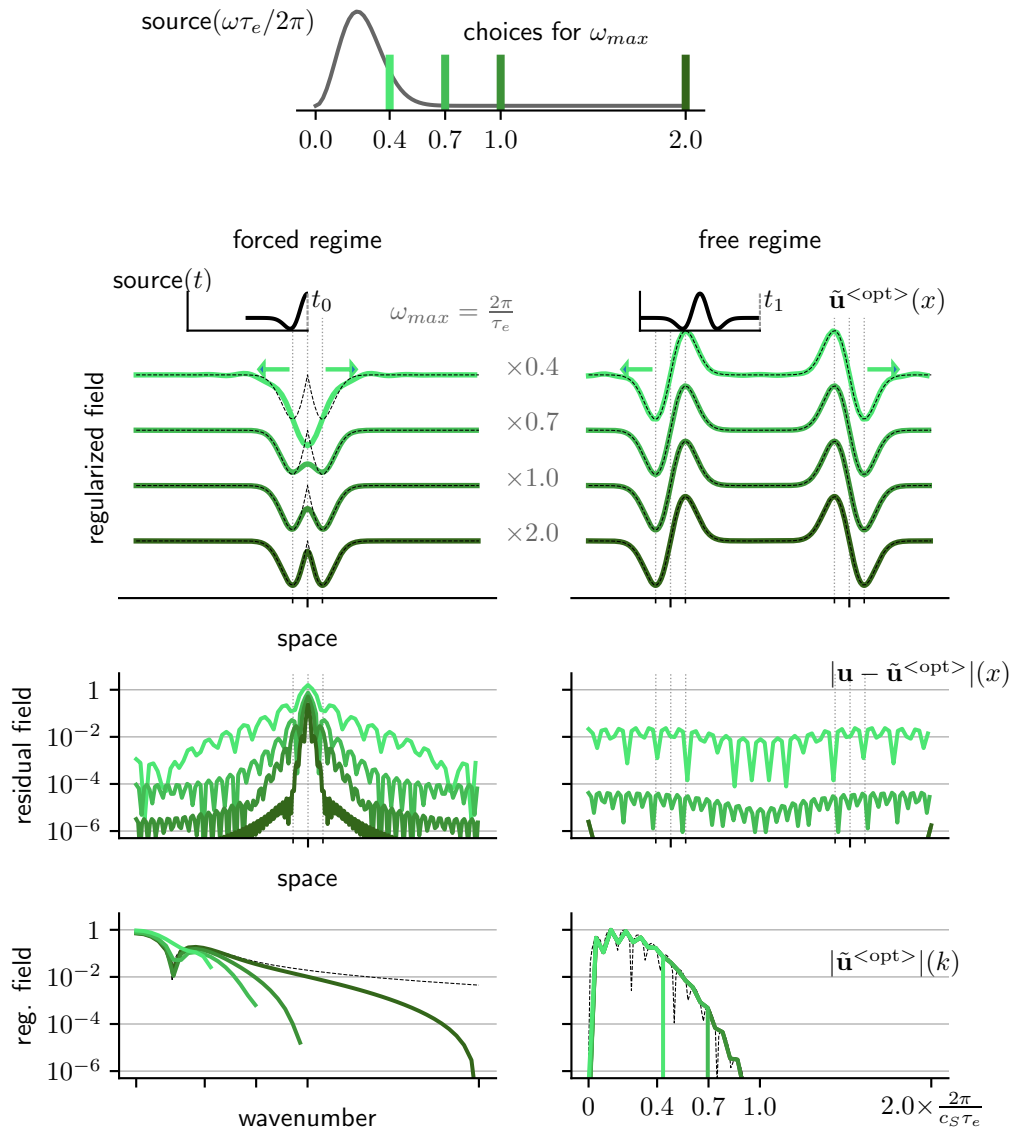

Figure 5: Regularized displacement of the SH_0 mode for several choices of the threshold ω_{max}. The exact field is represented in dotted line.

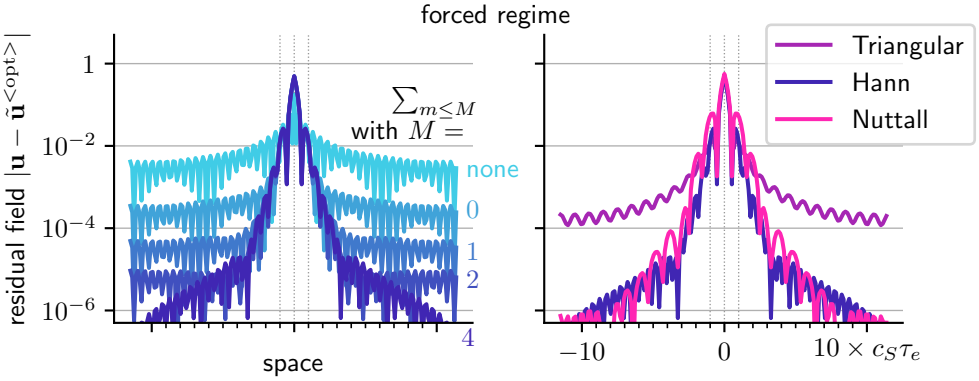

Figure 6: Influence on the residual field of the number of regularizing terms included in summation and of the smoothness of the window function.

lobes. Values of 10^{-5} for the residual field can be reached with a very fast exponential decrease with only 3 terms in the summation. However, if more accuracy is required, increasing the distance soon becomes less effective, and including more terms has less influence. Should the user demand deeper levels, a solution can be to switch to a smoother window such as Nuttall, although at the expense of tolerating a slower decrease at very short distances. These results are qualitatively maintained for other values of ω_{max} unless an exaggerated low threshold is decided. For instance, the value $0.4 \times 2\pi/\tau_e$ considered above first gives a decreasing behavior with m up to 4 terms, but then results in increasing spurious errors because Eq. (11) becomes a too coarse approximation.

Finally, let us close this section with a look at the other modes. The regularizing procedure is applied with 5 terms in summation (21), a Hann window for W and $\omega_{max} = 1 \times 2\pi/\tau_e \approx 25.1$ rad MHz. The Nyquist wavenumber is $k_{max}(\omega_{max}) \approx 8.4$ rad/mm. Actually, this time the modes with $\omega_n > \omega_{max}$ are not excluded so that the comparison may be performed with the branches SH_3 and upper, which entirely lay above 25.1 rad MHz. In a normal use, they are meant to be entirely excluded. The fields are evaluated at $z = z' = 0$ and represented in Fig. 7. Here again, the regularizing power of $\tilde{g}_n^{(S)}$ can be appreciated. Branches SH_3 and SH_{10} which were as high as 10^{-2} and 10^{-3} in the k domain and contributed to several tens of percent around $x = 0$ have been reduced by 4 and 9 orders of magnitude in the k domain. The reader may notice a sudden decrease on SH_1 and SH_2 branches slightly below k_{max} at $k \approx 7.9$ rad/mm and $k \approx 5.7$ rad/mm. These values correspond

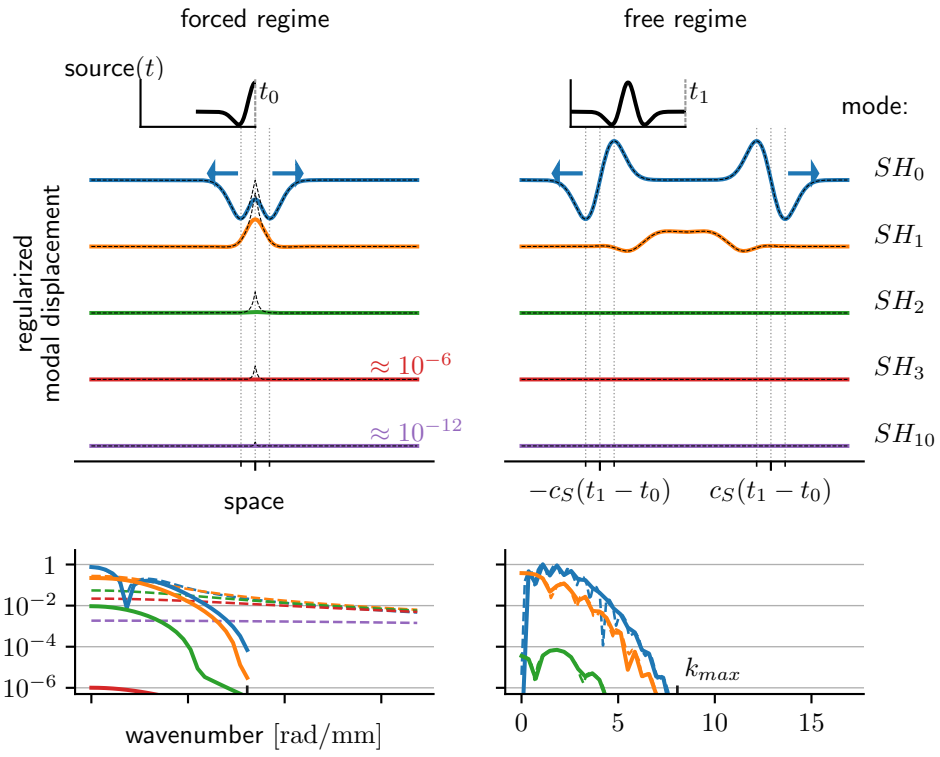

Figure 7: Regularized displacement of the first SH modes in the forced and free regimes computed by Fourier synthesis. The exact solution is represented in dotted lines.

to $\omega_1 = \omega_{max}$ and $\omega_2 = \omega_{max}$, *i.e.* $\Omega = 1$, and would normally be the bounds for excluding these modal contributions.

3.2.2. Example 2: transient P-SV motion

Let us take now an example that cannot be carried on analytically. The purpose is to point towards a more realistic case - although it is still canonical - in the sense that the developments of Section 3.1 will be applied to a modal basis obtained numerically, without needing to separate branches. The purpose is also to emphasize that a possible application to the regularization is to hybridize with a complementary evaluation of the field, which is the topic of the the last sections. For this reason, the spatial window will be deliberately chosen short enough to show space-periodization effects contaminating the results as soon as the fastest train reaches the edges.

Reference computations now rely on a (non-modal) method formulated in

the $\mathbf{k} - z - s$ domain, based on expanding the field over up- and down-going bulk waves in each layer of the plate (see for instance Refs. [12, 13, 14, 15, 16, 17]).

Modal computations now rely on a numerical evaluation of $(\omega_n, \mathbf{U}_n)(k)$ based on finding the eigensystem of a finite-difference matrix (see for instance Ref. [7]). It is in essence the same to what is commonly called "Thin Layer Method" [6] or "Semi Analytical Finite Elements". Time-convolutions could still be calculated analytically, but the Laplace domain is now preferred for convenience and to prepare for the next sections.

The medium and excitation signal are kept unchanged, but the force vector is now longitudinal. Furthermore, because the evaluation of the exact field now relies on a numerical Fourier synthesis, we take for a x dependency of $\mathbf{b}$ a thin but not perfectly point-wise function:

$$\mathbf{b}(x, z, t) = f(t) \, \frac{\mathrm{e}^{-x^2/2a^2}}{a\sqrt{2\pi}} \, \delta(z) \begin{pmatrix} 1 \\ 0 \\ 0 \end{pmatrix}. \tag{26}$$

The space-spectrum of $\mathbf{b}$ is then $\mathrm{e}^{-k^2a^2/2}$ and will be neglected after $K_{max} = 5/a$. K_{max} stands here for the Nyquist wavenumber of the exact calculation.

Two choices for ω_{max} will be made: $\omega_{max} = 1 \times 2\pi/\tau_e \approx 25.1$ rad MHz and $\omega_{max} = 0.7 \times 2\pi/\tau_e \approx 17.6$ rad MHz, representing high or moderate requirements of accuracy. k_{max} is found numerically for each of these thresholds as the solution to $\omega_0(k_{max}) = \omega_{max}$. We obtained $k_{max} \approx 9.1$ rad/mm and $k_{max} \approx 6.5$ rad/mm. The other parameters defining the regularization procedure will be kept constant: W is a Hann window and 5 terms will be included in summation (20).

The space-spectral extent of $\mathbf{b}$ is then set much wider than these values, so that truncating the Fourier integral at $|k| \leq k_{max}$ would generate a spatial aliasing during the forced regime. From now on we will take the numerical value $a = 0.125$ mm, which gives $K_{max} = 40$ rad/mm. Actually, the Nyquist wavenumber k_N slightly deviates from k_{max} in such a way that K_N/k_N is a rational number and both fields share the same k-grid (the modal evaluation being zero-padded for $k > k_N$) for an easier comparison. Figure 8 offers a summary.

The k-grid is set at $k = \{-K_{max} + \delta k, .., K_{max}\}$ in 400 steps, which gives a halved size of the space window $x_{max} \approx 15.7$ mm. The Laplace grid is defined with $t = \{0, .., t_{max} - \delta t\}$ in 80 steps with $t_{max} = 40\,\tau_e = 10$ μs,

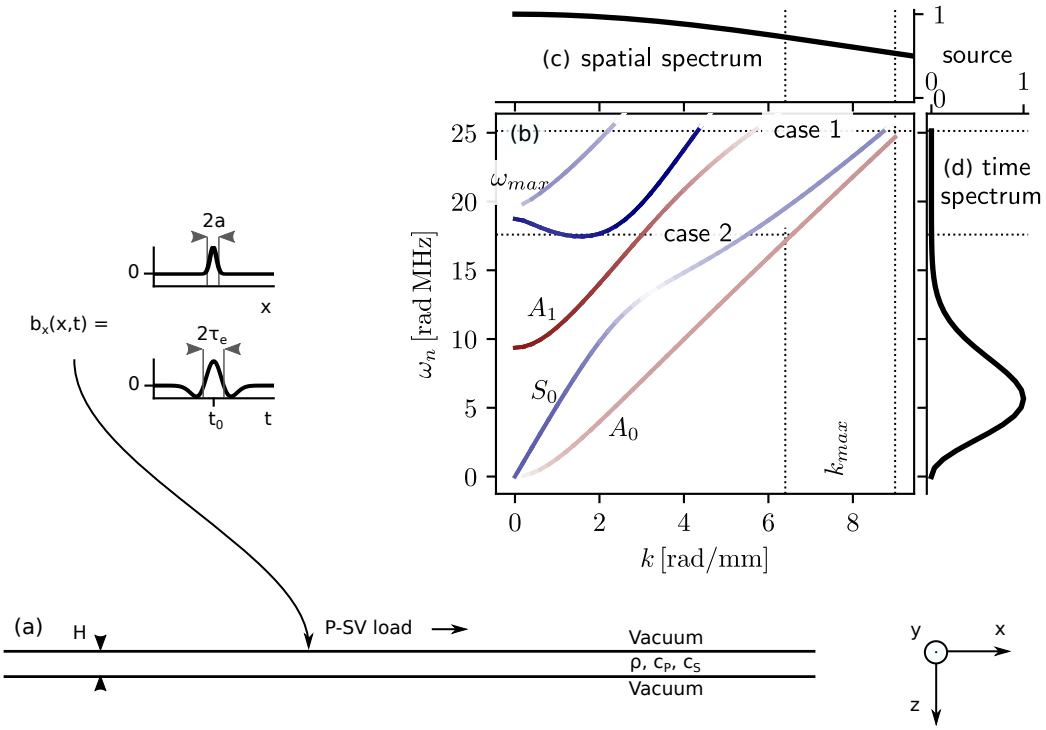

Figure 8: (a) Scheme of the configuration for the $P-SV$ examples. (b) First $P-SV$ Lamb modes of a 1 mm-thick aluminum plate, along with the (c) space- and (d) time-spectra of the longitudinal line load. In (b) the color intensity is proportional to the modal participation factor.

giving $\mathrm{Im}\{s\} = \{0, .., 2\pi/\tau_e\}$ in 41 steps, and the real part is set at $\mathrm{Re}\{s\} = 3.5\ \log 10/t_{max}$. The modes are obtained by discretizing the field into 19 points equally spaced between $z = 0$ and $z = H$ and by approximating ∂_z derivatives with a sixth order finite difference scheme. The goal pursued here is to ensure minimal errors from this step for proper comparisons with the exact method, rather than low costs.

The fields computed with the modal method will be superscripted $^{<\mathrm{opt}>}$. A tilde means that $\tilde{\mathbf{g}}^{(S)}$ has been subtracted to $\mathbf{g}$ whereas an absence of tilde means that the wavenumber integral has been truncated without applying the regularization step. An absence of superscript simply means that the field is exact, for having been computed using the non-modal method and sampled accordingly to the space-spectrum of the source. The fields are computed at the same depth ($z = z' = 0$). Only the x component will be monitored in

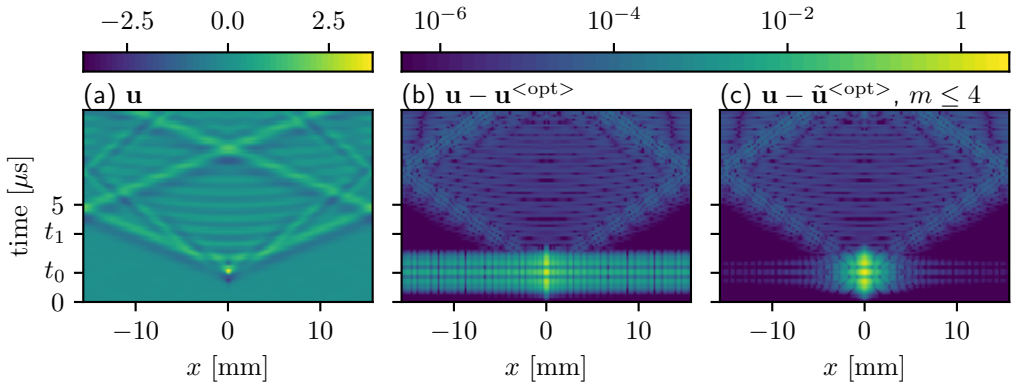

Figure 9: Case 1: space-time maps of: (a) the displacement field $\mathbf{u}$, (b) the residual field $\mathbf{u} - \mathbf{u}^{<\text{opt}>}$ without subtracting $\tilde{\mathbf{g}}^{(S)}$ to $\mathbf{g}$, (c) and $\mathbf{u} - \tilde{\mathbf{u}}^{<\text{opt}>}$, *i.e.* after subtracting $\tilde{\mathbf{g}}^{(S)}$ to $\mathbf{g}$. $\tilde{\mathbf{g}}^{(S)}$ allows to achieve a confinement of the residual field inside a small region near the source.

the figures, but the results are valid at the same level of accuracy for other components of the field or of the excitation.

The results obtained with $\omega_{max} = 1 \times 2\pi/\tau_e$ are presented in Fig. 9: (a) the (exact) displacement field produced by the source is most intense at ($x = 0$, $t = t_0$) when the source is maximal and then propagates in different modal trains: a S_0 one (fastest), a A_0 one (slower and a bit dispersive) and a A_1 one (slowest and most dispersive) can be identified. The maximal amplitude at $t = t_1 = 3.5$ μs (during the free regime) is used to normalize the fields, here and for every other figure further.

The residual field is shown in (b) without and (c) with application of the regularization step. As explained before $\mathbf{u}^{<\text{opt}>}$ suffers aliasing when the source is active, and this results into an intense and extended artifact. As soon as the source is zero, the only differences between $\mathbf{u}$ and $\mathbf{u}^{<\text{opt}>}$ stem from the error with which are obtained the eigenfrequencies and modeshapes (around 10^{-5} here)[6]. Concerning $\tilde{\mathbf{u}}^{<\text{opt}>}$, one can see (c) that its performance is qualitatively the same as in the previous examples. To give a more

[6]This error can be controlled arbitrarily by refining the depth-discretization and finite-difference order used to obtain the eigenvalue problem, as well as numerical methods used to calculate the norms and scalar products. A special care must be devoted to $\mathbf{k} = \mathbf{0}$, which should ideally be treated separately because rigid body modes $\omega_n = 0$ are usually obtained with high numerical errors. Here, we merely added a small non-zero part, *i.e.* $\mathbf{k} = \mathbf{0} + \boldsymbol{\epsilon}$, although this is not optimal.

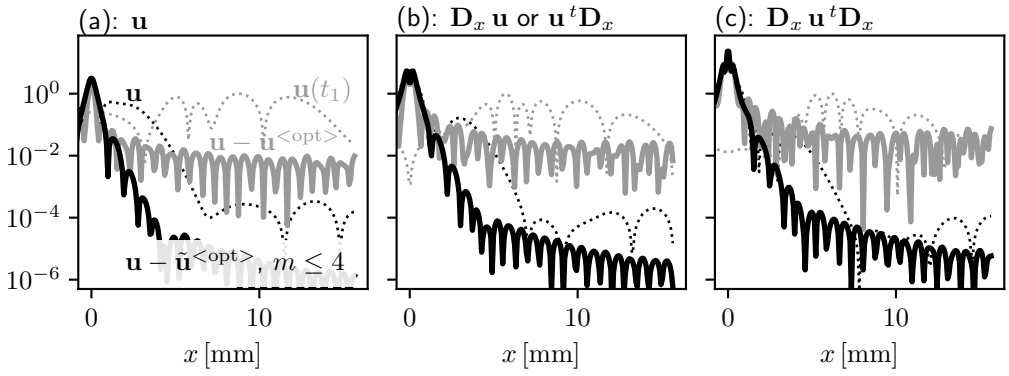

Figure 10: Residual fields for $\mathbf{u}$ and its derivatives at $t = t_0$, *i.e.* when the source term is maximal. As a reference for orders of magnitudes, the original field is shown in dotted lines at t_0 (forced regime) and $t_1 = 3.5\,\mu$s (free regime).

quantitative insight the fields are compared at t_0 in Fig. 10. We also show the comparison for the space derivatives, as they are of primary interest in a number of problems. We call $\mathbf{D}_x$ the longitudinal stress operator such as $\boldsymbol{\sigma}_x = \mathbf{D}_x\,\mathbf{u}$, and $\mathbf{D}_x^T$ its transpose such as $\mathbf{g}\,\mathbf{D}_x^T$ is the double-layer, or triadic, Green's tensor along x. As can be seen, $\tilde{\mathbf{u}}^{<\mathrm{opt}>}$ and its derivatives differ from the exact field within only a confined region (about 5 mm to reach 10^{-5} times the amplitude of the free regime, that is, about a S_0 wavelength at the operating frequencies).

These results are robust regarding the frequency content of the excitation and component of the field. Of course, a shorter or longer impulse produces an accordingly broader or thinner spot of residual field, but no matter whether broad band sources are involved (Gaussian impulses for instance): no rigid body problem appears and the quality shown here holds.

Let us close this section with a last example to make clear that ω_{max} has no influence on the precision with which are evaluated the time-convolutions. The first examples relied on an analytical formula. The former example relied on a numerical Laplace transform with $\mathrm{Im}(s)_{max} = \omega_{max}$. Here we set $\omega_{max} = 0.7\times 2\pi/\tau_e$, but we keep the s-grid unchanged with $\mathrm{Im}(s)_{max} = 2\pi/\tau_e$. The results are presented in Fig. 11. As can be seen, nothing unexpected appears but a higher background level (about 4×10^{-4}) due to neglected propagating modes.

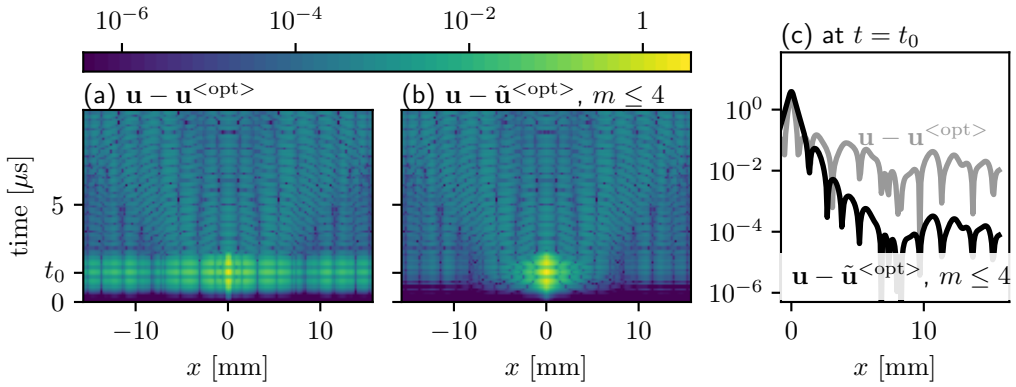

Figure 11: Case 2: residual fields without (a) or after (b) subtracting $\tilde{\mathbf{g}}^{(S)}$ to $\mathbf{g}$, and a comparison of both at the instant of maximal excitation. The only difference with case 1 is a higher background of errors due to a lower threshold ω_{max}.

4. Getting back the singular part on a separate grid

This section develops further on the second perspective mentioned in the introduction, namely the possibility of using $\tilde{\mathbf{g}}^{(S)}$ to combine the modal and non-modal approaches to compute the established and non-established regimes exactly, separately, and hence with a minimal sampling each, by restricting each formulation to the task on which it best performs.

4.1. Principle of the decomposition in two grids

Let us write:

$$\mathbf{u} = (\mathbf{u} - \tilde{\mathbf{u}}^{<\mathrm{opt}>}) + \tilde{\mathbf{u}}^{<\mathrm{opt}>}. \tag{27}$$

In Eq. (27) the right-hand $\tilde{\mathbf{u}}^{<\mathrm{opt}>}$ is meant to be computed on the whole domain of interest, that is, on presumably large distances and times, but with the sampling and modal truncation which is optimal for the free regime. There is nothing more to improve on this side. The sampling of $\mathbf{u} - \tilde{\mathbf{u}}^{<\mathrm{opt}>}$ must on the other hand be very fine according to the spatial spectrum of the source (the limit of a point excitation is out of reach without further hybridization, see Ref. [12, 13] to overcome it). However, according to the results of the previous section only a computation at short distances is necessary, which considerably reduces the overall cost. This principle is illustrated in Fig. 12. Furthermore, other savings can be made on the s grid by taking advantage of the memoryless nature of this field. This optimization is described below.

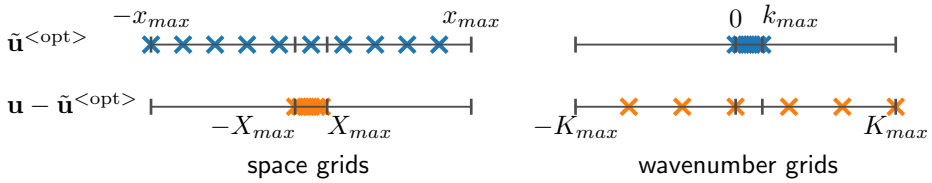

Figure 12: Schematic representation of the decomposition in two grids. The regularized propagating field is calculated on the whole domain of interest and sampled accordingly to the time-spectrum of the excitation, while the residual field is sampled accordingly to the space-spectrum of the load but calculated only in a few wavelenghts-large window.

4.2. Hybrid evaluation of the non-established regime in the Laplace domain using a memoryless expansion

The idea developed below is to expand the residual Green's tensor in a series of memoryless terms, that is, in the time domain in powers of time derivatives or in the Laplace domain in powers of s/ω_{max}. The intuition is that, after removing the propagating field, the remaining part consists of contributions of modes with frequencies higher than ω_{max}, plus spurious memoryless terms introduced by the regularization, plus memoryless contributions of low frequency modes that were not entirely captured by $\tilde{\mathbf{G}}^{(S)}$. All these contributions can in principle be well described by a power expansion such as Eqs. (10) or (11), so that one may be temped to try to exploit such a property.

We now focus only on the Laplace domain. As the wave equation is time-symmetric we keep only even powers. We write the following expansion:

$$\mathbf{G}-\tilde{\mathbf{G}}^{<\text{opt}>}=\Delta\tilde{\mathbf{G}}_0\left(\frac{s}{\omega_{max}}\right)^0+\Delta\tilde{\mathbf{G}}_2\left(\frac{s}{\omega_{max}}\right)^2+\ldots \tag{28}$$

Now the question is: how to obtain the basis $\Delta\tilde{\mathbf{G}}_{2m}$? We see no direct analytical answer. Still there is a simple numerical way out: it turns out to be enough to compute the residual Green's tensor at a small number of s samples and then solve a linear system:

$$\begin{bmatrix}1 & (s_1/\omega_{max})^2 & \ldots\\ 1 & (s_2/\omega_{max})^2 & \ldots\\ & \ldots & \end{bmatrix}\begin{bmatrix}\Delta\tilde{\mathbf{G}}_0\\ \Delta\tilde{\mathbf{G}}_2\\ \ldots\end{bmatrix}=\begin{bmatrix}(\mathbf{G}-\tilde{\mathbf{G}}^{<\text{opt}>})(s_1)\\ (\mathbf{G}-\tilde{\mathbf{G}}^{<\text{opt}>})(s_2)\\ \ldots\end{bmatrix}. \tag{29}$$

$\mathbf{G}-\tilde{\mathbf{G}}^{<\text{opt}>}$ is in this way obtained at all s as a post-treatment of a computation at only a few s samples.

Let us comment on the three choices that one has to make regarding system (29): is it the same to work in the space or in the Fourier domain, how to choose the order of the expansion, and how to choose the s_m samples best?

The first two answers are related. System (29) can be set either in the $\mathbf{k}$ domain, or on $\mathbf{u} - \tilde{\mathbf{u}}^{<\text{opt}>}$ in the $\mathbf{x}$ domain after the convolution with the source. Because of linearity, this might seem at first glance of no importance, although the former option is better as it allows for even more savings. Indeed, as illustrated in Fig. 13, the order of the expansion in powers of $(s/\omega_{max})^2$ may be adapted with $\mathbf{k}$. Below k_{max} at least the same order as used to build $\tilde{\mathbf{g}}^{(S)}$ is necessary, because $\tilde{\mathbf{g}}^{(S)}$ introduces spurious extra time derivative terms when $\tilde{\omega}_{nm} \neq \omega_n$. But beyond k_{max} this is no longer the case because $\tilde{\mathbf{G}}^{(S)}(||\mathbf{k}|| > k_{max}) = \mathbf{0}$, and the needs go decreasing. This can again be explained with Eq. (11): the higher ω_n, the lower $(s/\omega_n)^{2m}$, and as long as ω_n is asymptotically a linearly growing function of $\mathbf{k}$: the higher $||\mathbf{k}||$, the lower m needs to be for a given level of accuracy.

The third answer is as follows: in order to maximize the determinant of the Vandermonde matrix, s_m should be chosen with an imaginary part equally spaced between 0 and ω_{max}. Let us highlight that the bound of this interval refers to the truncation of the modal basis and not to half the sampling frequency of the excitation signal, which may be greater. Indeed, one should keep in mind that $\tilde{\mathbf{G}}^{(S)}$ was designed to capture the singular behavior in the limit $|s| \ll \omega_{max}$, so if $\text{Im}(s_m)$ are chosen greater than ω_{max}, then system (29) favors higher powers of $(s/\omega_{max})^{2m}$ more than they should be. To end up with this point let us comment on $||\mathbf{k}|| > k_{max}$: beyond this threshold $\mathbf{G}$ has no pole $|\omega_n| \leq \omega_{max}$, so s_m can in principle be chosen pure imaginary, if desired.

4.3. Illustration on a $P - SV$ example

As an illustration we take again for example the $P - SV$ configuration of Section 3.2.2 with $\omega_{max} = 2\pi/\tau_e$. We use the same parameters to obtain the modal basis and to build $\tilde{\mathbf{G}}^{(S)}$, the same k-grid, the same value for the Nyquist Laplace variable $\text{Im}(s)_{max} = 2\pi/\tau_e$ and the same real part. The only difference is that now the s-grid has 5 steps instead of 41: $\delta\text{Im}(s) = \text{Im}(s)_{max}/4$. At each k of the grid $\mathbf{G}(z, z')$ is computed using the non-modal method at the five s points, and if $|k| < k_{max}$ then $\tilde{\mathbf{G}}^{<opt>}$ is also computed and subtracted to it. System (29) is then constructed and solved to obtain $(\Delta\tilde{\mathbf{G}}_0, \Delta\tilde{\mathbf{G}}_2, ..., \Delta\tilde{\mathbf{G}}_8)(k)$ (see Fig. 13). Finally, the 41 points of the

original s-grid are deduced using Eq. (28) and k is incremented. Once this procedure has been applied for all k, convolutions are calculated by multiplying $\mathbf{G}-\tilde{\mathbf{G}}^{<opt>}$ with the spectra of the source and the inverse Fourier and Laplace transforms are applied to obtain the residual field $\mathbf{u}-\tilde{\mathbf{u}}^{<opt>}$ on the 400×80 space-time grid. The results are represented in Figure 14 and compared to those obtained without relying on the memoryless expansion, that is, after a usual calculation at the 41 points of the s-grid. One can see that the only remaining differences (10^{-5} times the amplitude in the free regime) stem from the level of accuracy with which are obtained the modes. As commented above, the expansion does not require so high orders for $|k| > k_{max}$: indeed, we maintained the same level of errors with the following adaptive truncation (see Fig. 15): $m \leq 4$ for $|k| \leq k_{max}$ and $\delta\mathrm{Im}(s) = \mathrm{Im}(s)_{max}/4$, then $m \leq 2$ for $k_{max} < |k| \leq 2\,k_{max}$ and $\mathrm{Im}(s) = (0, \pi/\tau_e, 2\pi/\tau_e)$, and finally $m = 0,\ 1$ for $|k| > 2\,k_{max}$ and $\mathrm{Im}(s) = (0, 2\pi/\tau_e)$. These thresholds on k are purely empirical. They are probably slightly exaggerated because the excitation is not perfectly white in space but decreases with large k, which helps minimizing additional errors due to this adaptive truncation. Nevertheless, this means that only two computations of $\mathbf{u}$ are needed on the potentially big spectral k-grid to achieve a similar numerical accuracy as with a computation at all s. If the singular field is wanted at several tens or hundreds of time steps, this is a gain of one to two orders of magnitude in computational resources.

5. Summary

Along with standard steps, the developments presented in this article can be assembled in sequences summarized as follows. Given a layered plate, given a load $\mathbf{b}(\mathbf{x}, z, t) = f(t)\,\boldsymbol{\psi}(\mathbf{x}, z)$ having a time-history f of finite spectral extent and a spatial distribution $\boldsymbol{\psi}$ potentially perfectly point-wise, and given a spatial domain of interest $[-x_{max}, x_{max}] \times [-y_{max}, y_{max}]$, the resulting displacement field $\mathbf{u}(\mathbf{x}, z, t)$ can be separated into a smooth, propagating field $\tilde{\mathbf{u}}$ (called established regime), and a sharp, non-propagating residual field $\mathbf{u} - \tilde{\mathbf{u}}$ (called non-established regime). $\tilde{\mathbf{u}}$ and $\mathbf{u} - \tilde{\mathbf{u}}$ are evaluated on distinct spatial grids. Eventually, the sum $\mathbf{u} = \tilde{\mathbf{u}} + (\mathbf{u} - \tilde{\mathbf{u}})$ can be done by relying on zero-padding or other usual interpolation techniques.

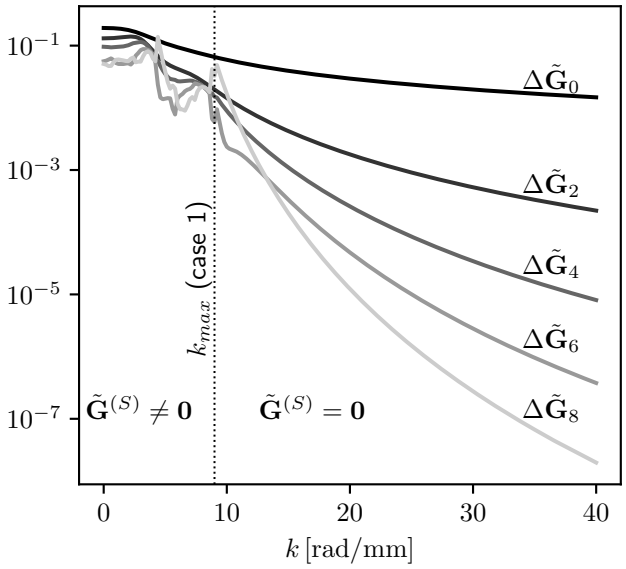

Figure 13: Outcome of system (29) for the configuration of Section 3.2.2: magnitudes of the terms of the basis used to expand the residual field. Below $||\mathbf{k}|| \leq k_{max}$ the same order m as in summation (20) is needed, but higher orders become soon insignificant beyond $||\mathbf{k}|| > k_{max}$. In the limit $||\mathbf{k}|| \gg k_{max}$ only two terms are enough, and only the static one $\Delta\tilde{\mathbf{G}}_0$ at $||\mathbf{k}|| \ggg k_{max}$.

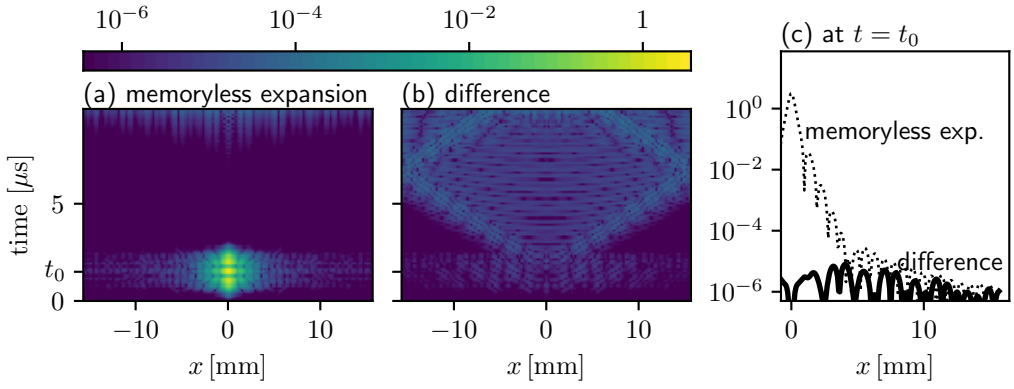

Figure 14: (a) Memoryless expansion (see Eq. (28)) based computation of $\mathbf{u} - \tilde{\mathbf{u}}^{<\text{opt}>}$, (b) and (c) comparison with a computation on the full s grid.

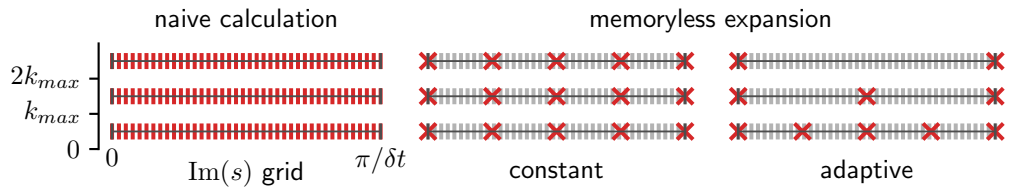

Figure 15: Schematic representation of the grid for the Laplace variable: red markers stand for points actually computed and grey ones for points post-treated from red ones

5.1. Calculation of the established regime

- Decide on the angular frequency ω_{max} above which the spectrum of the time-history f can be neglected. Defining this criterion implicitly sets the spatial sampling for the established regime, independently of the spatial distribution $\boldsymbol{\psi}$.

- Calculate the modeshapes $\mathbf{U}_n(\mathbf{k})$ and angular eigenfrequencies $\omega_n(\mathbf{k})$ of the plate to obtain $\mathbf{G}(\mathbf{k}, z, t)$ using Eq. (5). Do it at each point $\mathbf{k}$ of a grid $\{-k_{x,max} + \delta k_x, .., k_{x,max}\} \times \{-k_{y,max} + \delta k_y, .., k_{y,max}\}$ defined by the steps $\delta k_x = \pi / x_{max}$, $\delta k_y = \pi / y_{max}$ and by the upper bounds $k_{x,max}$ and $k_{y,max}$ to be specified. Keep only the modes below the frequency threshold: $\omega_n(\mathbf{k}) < \omega_{max}$. The Nyquist wavenumbers $k_{x,max}$ and $k_{y,max}$ are the lowest values at which the first mode is above the frequency threshold: $\omega_0(\mathbf{k}) \geq \omega_{max}$. Use the symmetry $(\mathbf{U}_n, \omega_n)(-\mathbf{k}) = (\mathbf{U}_n^*, \omega_n^*)(\mathbf{k})$ (complex conjugation) to reduce the spectral grid to half of its points. Naturally, if the medium is isotropic or planar isotropic, then the modes only depend on the radial wavenumber $k = |\mathbf{k}|$ and additional savings can be made.

- Calculate the modal participation factors from the spatial distribution of the load: $\Psi_n(\mathbf{k}) = \int_0^H \mathbf{U}_n^\dagger \, \boldsymbol{\Psi} \, \mathrm{d}z$, with $\boldsymbol{\Psi}(\mathbf{k}, z) = \mathcal{F}\{\boldsymbol{\psi}(\mathbf{x}, z)\}$ the 2D-space-Fourier transform of $\boldsymbol{\psi}$.

- Introduce the regularizing term $\tilde{g}_n^{(S)}(t)$ using Eqs. (20) (or (21)), (23) and (24) to subtract the contribution of the non-established regime to the modal propagator $g_n(t)$ (see Eq. (6)), and calculate the time convolutions $\tilde{f}_n(t) = (g_n - \tilde{g}_n^{(S)}) * f$.

- Calculate the regularized response in the $k{-}z{-}t$ domain at the required depth z: $\tilde{\mathbf{U}}(\mathbf{k}, z, t) = \sum_n \Psi_n \, \tilde{f}_n(t) \, \mathbf{U}_n(z)$.

- Finally, obtain the regularized (established) response in the physical domain by numerically calculating the inverse spatial Fourier transform: $\tilde{\mathbf{u}}(\mathbf{x}, z, t) = \mathcal{F}^{-1}\{\tilde{\mathbf{U}}(\mathbf{k}, z, t)\}$. This field perfectly coincides with the "true" response $\mathbf{u}(\mathbf{x}, z, t)$ except in a close neighborhood of the load whose radius is a few space samples large (*i.e.* $\propto \pi/k_{x,y,max}$) and is controlled by ω_{max}.

5.2. Calculation of the non-established regime

The procedure summarized here makes the additional hypothesis that the spatial distribution of the load $\boldsymbol{\psi}$ has a finite spectral extent.

- Decide on how far from the load the residual field $\mathbf{u} - \tilde{\mathbf{u}}$ is small enough to be neglected, and set the size of the spatial domain of interest to this corresponding window, called: $[-X_{max}, X_{max}] \times [-Y_{max}, Y_{max}]$. This defines the wavenumber steps $\delta K_x = \pi/X_{max}$ and $\delta K_y = \pi/Y_{max}$. As commented above, $X_{max} \propto \pi/k_{x,max}$ and $Y_{max} \propto \pi/k_{y,max}$. To set ideas, in case 1 of Sec. 3.2.2 taking $X_{max}\, k_{x,max}/\pi \approx 10$ means neglecting relative contributions of 10^{-4}.

- Decide on the wavenumbers $K_{x,max}$ and $K_{y,max}$ above which the 2D-spectrum of $\boldsymbol{\psi}$ can be neglected. These thresholds define the spatial sampling for the non-established regime, independently of the time-history f, its frequency extent ω_{max}, and the Nyquist wavenumbers for the established regime $k_{x,y,max}$. Should $\boldsymbol{\psi}$ be extremely sharp, or perfectly point-wise, then $K_{x,y,max}$ may be uncontrollably high, the number of points in the grid may still be very large and computations intractable despite the savings listed below. This case is not covered by this article and the reader is referred to Refs. [12, 13].

- At each point $\mathbf{k}$ of the grid $\{-K_{x,max} + \delta K_x, .., K_{x,max}\} \times \{-K_{y,max} + \delta K_y, .., K_{y,max}\}$ calculate the residual field $(\mathbf{U} - \tilde{\mathbf{U}})(\mathbf{k}, z, s)$ at the required depth z and at a few points s (Laplace parameter) in order to build system (29). $\tilde{\mathbf{U}}$ is computed using the modal expansion and regularizing term as explained above and is non-zero only for $|k_x| < k_{x,max}$ and $|k_y| < k_{y,max}$, while $\mathbf{U}$ is computed using a non-modal formulation. As $||\mathbf{k}||$ increases less s points are needed.

- At each point $\mathbf{k}$, solve system (29) and use Eq. (28) to deduce $(\mathbf{U} - \tilde{\mathbf{U}})(\mathbf{k}, z, s)$ at the other points of a s grid.

- Perform the inverse Fourier transform $\mathcal{F}^{-1}$ to go back to the spatial domain, and the inverse Laplace transform $\mathcal{L}^{-1}$ to go back to the time domain: $(\mathbf{u} - \tilde{\mathbf{u}})(\mathbf{x}, z, t) = \mathcal{L}^{-1}\{\mathcal{F}^{-1}\{(\mathbf{U} - \tilde{\mathbf{U}})(\mathbf{k}, z, s)\}\}$.

6. Conclusion

In this article, a tensor with the same singular behavior as the Green's tensor has been introduced in the wavenumber-time and in the wavenumber-Laplace domains and expressed in the basis of the Lamb modes. Its performance as a regularizing term have been demonstrated numerically. It allows recovering an operative separation between near and far field as with propagative and evanescent modes, although such concepts do not exist in a causal formalism. This achievement is reached at the cost of dealing with a quantity defined with some arbitrariness, although the parameters highlighted to construct it enable stable results and do not need to be tuned for every new situation. Two applications were emphasized. First, subtracting this regularizing tensor to the Green's tensor enables to synthesize the propagative field radiated by a true point source using the wavenumber-time domain modal expansion, even during the excitation regime and without spatial aliasing artifacts. Second, a hybrid method was suggested to efficiently compute the non-propagative remaining part of the field radiated by a thin - although not perfectly point-wise - source by combining with a non-modal method also formulated in the wavenumber domain. Optimizations were highlighted to benefit from the property of this residual field to allow an efficient representation in a series of positive entire powers of the frequency. The outcome is a decomposition of the field on two numerical Fourier grids: a large and optimally coarse grid for the far field, to be computed on the entire Laplace grid, plus a small, very thin grid, asymptotically only needed at two points of the Laplace grid. These developments may particularly find applications in three dimensional and anisotropic problems for which optimizing the grids is a critical issue. Moreover, it may become affordable to solve time domain scattering problems by building a boundary element method relying on a hybrid computation of the Green's tensor as presented here.

Acknowledgements

The author acknowledges E. Ducasse (ENSAM) for his comments and help on the terminology. The two anonymous reviewers are also gratefully acknowledged.

References

[1] B. A. Auld, Acoustic fields and waves in solids, Vol. 2, New York: J. Wiley and Sons, 1973.

[2] A. Velichko, P. D. Wilcox, Modeling the excitation of guided waves in generally anisotropic multilayered media, The Journal of the Acoustical Society of America 121 (1) (2007) 60–69. doi:10.1121/1.2390674.

[3] E. Glushkov, N. Glushkova, A. Eremin, Forced wave propagation and energy distribution in anisotropic laminate composites, The Journal of the Acoustical Society of America 129 (5) (2011) 2923–2934. doi:10.1121/1.3559699.

[4] A. Karmazin, E. Kirillova, W. Seemann, P. Syromyatnikov, A study of time harmonic guided Lamb waves and their caustics in composite plates, Ultrasonics 53 (1) (2013) 283 – 293. doi:10.1016/j.ultras.2012.06.012.

[5] M. Stévenin, A. Lhémery, S. Grondel, An efficient model to predict guided wave radiation by finite-sized sources in multilayered anisotropic plates with account of caustics, in: Journal of Physics: Conference Series, Vol. 684, IOP Publishing, 2016, p. 012004.

[6] E. Kausel, Thin-layer method: Formulation in the time domain, International Journal for Numerical Methods in Engineering 37 (6) (1994) 927–941. doi:10.1002/nme.1620370604.

[7] E. Ducasse, M. Deschamps, Time-domain computation of the response of composite layered anisotropic plates to a localized source, Wave Motion 51 (8) (2014) 1364 – 1381. doi:10.1016/j.wavemoti.2014.08.003.

[8] A. Romero, P. Galvín, A BEM-FEM using layered half-space Green's function in time domain for SSI analyses, Engineering Analysis with Boundary Elements 55 (2015) 93 – 103. doi:10.1016/j.enganabound.2014.11.027.

[9] J. Park, E. Kausel, Impulse response of elastic half-space in the wave number - time domain, Journal of Engineering Mechanics 130 (10) (2004) 1211–1222. doi:10.1061/(ASCE)0733-9399(2004)130:10(1211).

[10] J. Park, E. Kausel, Response of Layered Half-Space Obtained Directly in the Time Domain, Part I: SH Sources, Bulletin of the Seismological Society of America 96 (5) (2006) 1795–1809. doi:10.1785/0120050246.

[11] E. Kausel, J. Park, Response of Layered Half-Space Obtained Directly in the Time Domain, Part II: SV-P and Three-Dimensional Sources, Bulletin of the Seismological Society of America 96 (5) (2006) 1810–1826. doi:10.1785/0120050247.

[12] E. Kausel, Advanced structural dynamics, Cambridge University Press, 2017.

[13] E. Kausel, Generalized stiffness matrix method for layered soils, Soil Dynamics and Earthquake Engineering 115 (2018) 663–672. doi:10.1016/j.soildyn.2018.09.003.

[14] E. Kausel, J. M. Roesset, Stiffness matrices for layered soils, Bulletin of the Seismological Society of America 71 (6) (1981) 1743–1761.

[15] H. Schmidt, G. Tango, Efficient global matrix approach to the computation of synthetic seismograms, Geophysical Journal International 84 (2) (1986) 331–359. doi:10.1111/j.1365-246X.1986.tb04359.x.

[16] M. J. S. Lowe, Matrix techniques for modeling ultrasonic waves in multilayered media, IEEE Transactions on Ultrasonics, Ferroelectrics, and Frequency Control 42 (4) (1995) 525–542. doi:10.1109/58.393096.

[17] P. Mora, E. Ducasse, M. Deschamps, Transient 3D elastodynamic field in an embedded multilayered anisotropic plate, Ultrasonics 69 (2016) 106–115. doi:10.1016/j.ultras.2016.03.020.

[18] W. T. Thomson, Transmission of elastic waves through a stratified solid medium, Journal of Applied Physics 21 (2) (1950) 89–93. doi:10.1063/1.1699629.

[19] N. A. Haskell, The dispersion of surface waves on multilayered media, Bulletin of the Seismological Society of America 43 (1) (1953) 17–34.

[20] E. Kausel, J. M. Roesset, Frequency domain analysis of undamped systems, Journal of Engineering Mechanics 118 (4) (1992) 721–734. doi:10.1061/(ASCE)0733-9399(1992)118:4(721).

[21] J. Achenbach, Wave Propagation in Elastic Solids, North-Holland Series in Applied Mathematics and Mechanics, Elsevier, Amsterdam, 1975.